Optics and Lasers in Engineering 163 (2023) 107472

Contents lists available at ScienceDirect

Optics and Lasers in Engineering

journal homepage: www.elsevier.com/locate/optlaseng

Metasurface-based polarization color routers

Xiujuan Zou [a], Guangxing Gong [a], Yu Lin [b], Boyan Fu [a], Shuming Wang [a,c,d,*], Shining Zhu [a,c,d], Zhenlin Wang [a,d,*]

[a] National Laboratory of Solid State Microstructures, School of Physics, Nanjing University, Nanjing 210093, China
[b] Key Laboratory of Nanodevices and Applications, Suzhou Institute of Nano-Tech and Nano-Bionics, Chinese Academy of Science, Suzhou 215123, China
[c] Key Laboratory of Intelligent Optical Sensing and Manipulation, Ministry of Education, Nanjing University, Nanjing 210093, China
[d] Collaborative Innovation Center of Advanced Microstructures, Nanjing 210093, China

ARTICLE INFO

Keywords:
Metasurface
Color router
Polarization

ABSTRACT

Polarization, an attribute of light, carries a lot of vital information independent of intensity and color content. Polarization imaging is very useful in applications including diffuse/specular component separation, material classification and reflectance estimation. Color routers applied in color imaging provide an efficient way to sort and guide different color lights to the corresponding output ports. Here, we report the design and experimental realization of a compact metasurface-based polarization color router. This color router shows a micron Bayer pattern (RGGB distribution) under the illumination of white light with any polarization. In addition, the green light intensity at the corresponding pixel changes regularly depending on the polarization light, illustrating the polarization color router can act as a polarizer at the same time. The measured light utilization efficiency of the polarization color router reaches a value of 88%. A correlation coefficient of 0.98, which is defined as the fitting effect between the measured and theoretical illuminating light polarization angles, was achieved. This device possesses the advantages of a lightweight, high light utilization efficiency and polarization-integrated detection functions, which could provide a new way for its applications in integrated CMOS image sensors.

1. Introduction

Metasurface-based color router (MCR), which can combine focusing and sorting functions, provides a significant high light-harvesting efficiency owing to its working principle of sorting color rather than filtering light [1–4]. MCR is extremely appealing in applications that integrate multiple functions together with the requirement of the device's integration and miniaturization [5]. MCRs are anticipated to be useful in digital color imaging sensors to compensate for some of the shortcomings of current color filters [1,3,6]. Several designs of color routers based on nanostructures or metasurfaces have been recently reported using different approaches [6–11]. So far, MCRs have met several criteria for modern color image sensors, including high light utilization, excellent color sensitivity, high structural integration, and pixel sizes of less than a micron.

In addition to color and intensity attributes, polarization is another important property of light that describes the oscillation orientation of the transverse electric field along the optical path. Polarization generation using metasurface has attracted large attention in recent years [12–18]. Using the geometric phase [19–21], propagation phase [14,22], or a combination strategy for the control of a pair of independent phase profiles is a common method of realizing polarization-dependent devices [23–25]. This capability allows for various compact polarization-dependent metasurface-based devices with photonic functionalities [26,27], such as multichannel hologram display [15,28-30], orbital angular momentum state generators [30–35], and polarization imaging [22,36,37]. Among them, polarization imaging is widely used in industrial inspection in recent years, such as diffuse/specular component separation [38], material classification [39], reflectance estimation [40], etc. Thus, integrated metasurface-based polarizers [41,42] or polarization routers [43] are desired to achieve effective extraction of invisible information for polarized imaging in some special environments.

The color router mentioned above usually works only under a specific polarization. In this work, we design and experimentally demonstrate a metasurface-based polarization color router (MPCR) motivated for use in a commercial CMOS image sensor with a pixel pitch of 1 μm under any polarization. In addition to its ability to capture brightness and color with a high spatial resolution, our polarization router can capture polarization information, thus simultaneously

* Corresponding authors.
E-mail addresses: wangshuming@nju.edu.cn (S. Wang), zlwang@nju.edu.cn (Z. Wang).

https://doi.org/10.1016/j.optlaseng.2022.107472
Received 2 November 2022; Received in revised form 6 December 2022; Accepted 29 December 2022
Available online 5 January 2023
0143-8166/

acquiring both color and polarization information of a scene. By measuring the intensity of green pixels, the polarization orientation of incoming light can be well reproduced.

2. Designs and results

The design concepts of our color router and common color filters are shown in Fig. 1(a), respectively. Color routers guide all the incident light transmitted through the metasurface to different color pixels according to different wavelengths, while color filters are usually band-pass and waste the energy outside the expected waveband. Fig. 1(b) shows the schematic of a color image sensor employing MPCRs under the illumination of horizontally (i.e., along the x-axis) polarized light. Here, the metasurface is designed by the optimization method of genetic algorithm (GA) [44,45]. An area of 2 μm × 2 μm of a unit cell is selected to conform to the pixel level of the state-of-art CMOS image sensor. The unit cell is divided into a 20×20 grid, with each square denoting either an air column or a silicon nitride (Si_3N_4) column. Because Si_3N_4 has a reasonably high refractive index, negligible absorption in the visible band, and compatibility with CMOS technology, it was chosen after careful consideration. The thickness of the metasurface is set as 600 nm to guarantee the aspect ratio that can be prepared in current fabrication technology and the sufficient equivalent refractive index. We will show that the MPCR can enable the incident light sorted to target color pixels. In addition, the intensity of green pixels is demonstrated to depend on the polarization orientation of incoming light and thus can be used to determine the illuminating light polarization. The dark areas in some green photodetectors shown in Fig. 1(b) are ascribed to the effect of the MPCR due to a horizontal polarization state of incident light.

The metasurface is designed inversely using the GA method [7,30–32], which iteratively generates a two-dimensional pattern to optimize a specified objective function. Here, the GA toolbox in Matlab and commercial Lumerical FDTD solutions software is combined to optimize the structural distribution of the metasurface. Thus, the binary distributions of nanostructures in the metasurface are expressed as the basic variable of optimization, and the transmittances of four quadrants corresponding to RG_1G_2B pixels (i.e., a red, two green and a blue pixel) are regarded as the fitness values of optimization. In the optimization process shown in Fig. 2(a), the first step is to initialize the first population according to the number of variables. The coordinate coding is then carried out in FDTD by transforming the binary sequences in GA into nanopillars with different materials (Si_3N_4 or air) at different positions of the metasurface. When the model is built, the transmittances of RGGB pixels are calculated. The fitness value of each individual is calculated according to the transmittances and the fitness function as follows:

$$F = -\left(a_1 \int_{\lambda_{r1}}^{\lambda_{r2}} T_R d\lambda + a_2 \int_{\lambda_{g1}}^{\lambda_{g2}} T_{G1} d\lambda + a_3 \int_{\lambda_{b1}}^{\lambda_{b2}} T_B d\lambda - a_4 \int_{\lambda_{g1}}^{\lambda_{g2}} T_{G2} d\lambda\right), \tag{1}$$

where λ_{c1} and λ_{c2} are the minimum and maximum wavelengths and C represents R, G or B color waveband (600 nm-700 nm for R, 500 nm-600 nm for G_1 and G_2, and 400 nm-500 nm for B), respectively. In Eq. (1), a_c is the weight of the integral of the transmittance in each pixel. T_R, T_{G1}, T_{G2} and T_B are the transmittances of R, G_1, G_2 and B pixels, respectively. In the fitness function, the T_R, T_{G1} and T_B are *expec*ted to be enlarged in each color waveband and T_{G2} to be reduced during the optimization process, which is the key to polarization response. The individuals of the current generation are sorted by the calculated fitness values according to the formation of $P_i = F_i^2/\sum F_i^2$, and the individuals who behave better are more likely to be selected and reserved. A new generation of the population was then created through mutation and crossover operators. The stop criterion is that the fitness of the best individual reaches the average fitness of the current generation within 20 generations. Detailed information on the optimization process is shown in Section 1 in **Supplementary Materials**. Figs. 2(b-d) show the distribution changes of nanostructures within a unit cell and the spectral response corresponding to the structural distribution during the iteration process. Fig. 2(b) depicts an initial individual with a poor spectral response and averaged sorting efficiencies of three color bands of 29%. Sorting efficiency is defined as the averaged spectral efficiency, which is represented by a color line in the graphs for the corresponding color band. In Fig. 2(c), a nearly half-optimized individual with spectral responses meets the requirements for red and blue pixels but not for green pixels. The average efficiency of the three color bands is 34%. Fig. 2(d) shows the final optimized individual, which shows that all spectrum responses of RGGB pixels meet the objectives. And the average efficiency of the three color bands is 42%, which is greater than Bayer filters.

According to the final optimized metasurface, we simulated the spectral efficiencies of four pixels with the illumination of broadband linearly polarized light, as shown in Fig. 3(a). It shows that the averaged efficiencies of the RG_1B pixels over the whole pixel area are 39%, 42% and 58% at wavelengths of 430 nm, 530 nm and 680 nm, respectively, which greatly exceeds the ideal efficiency of the color filters (~33%) in the image sensor. In addition, the efficiency of the other green pixel

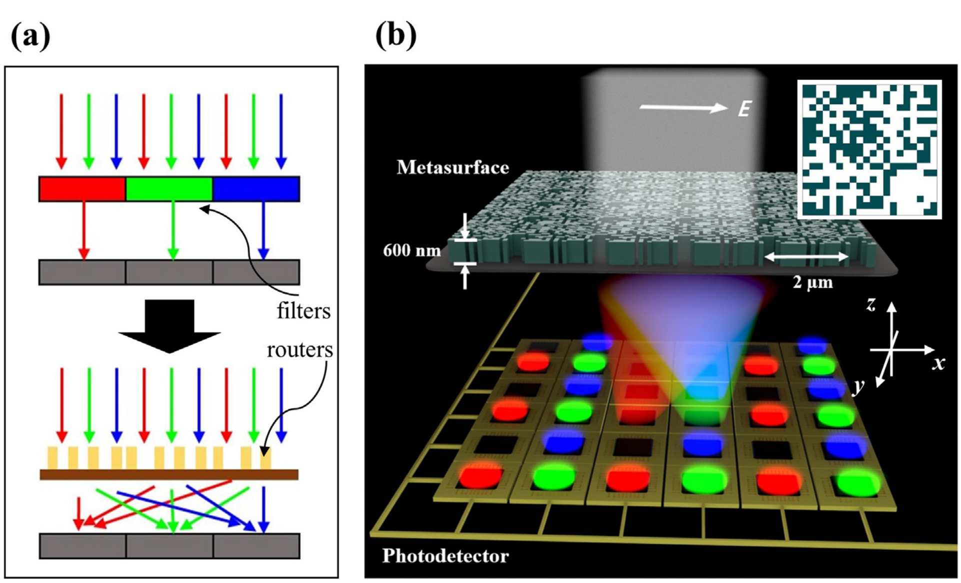

Fig. 1. (a) Differences in principle between conventional color filters and color routers based on metasurfaces. (b) Schematic of a color image sensor by employing MPCRs, where all the linearly polarized light can reach photodetectors in theory. Horizontally or vertically polarized light can be collected by the photodetector of one green pixel in a unit cell, whereas the other green pixel in the unit cell detects nearly no green light. Inset: the nanostructure distribution of the optimal solution of the MPCR.

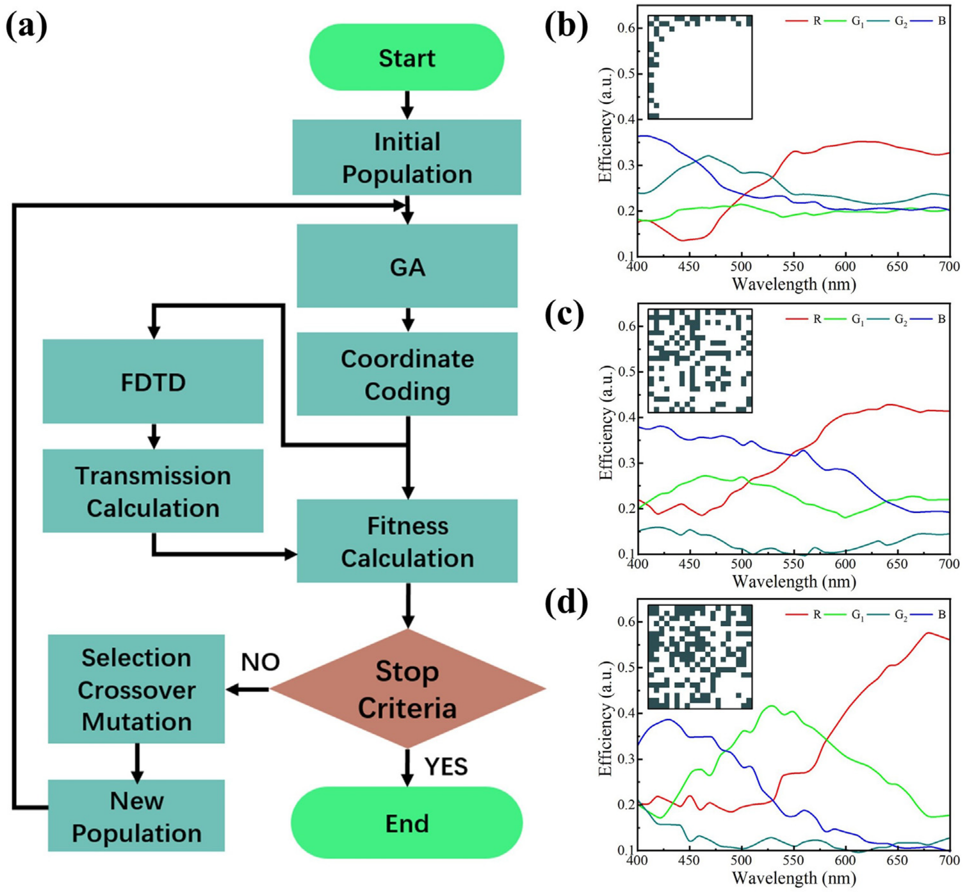

Fig. 2. (a) flowchart of the inverse design approach that combines the GA and FDTD. (b-d) The variation of spectral efficiencies and the individual nanostructure pattern (the inset) during the iteration processes. The color of each curve in these figures represents the spectral efficiency of the corresponding pixel that collects the color-band light. (b) The initial individual. (c) The nearly half-optimized individual. (d) The final optimized individual.

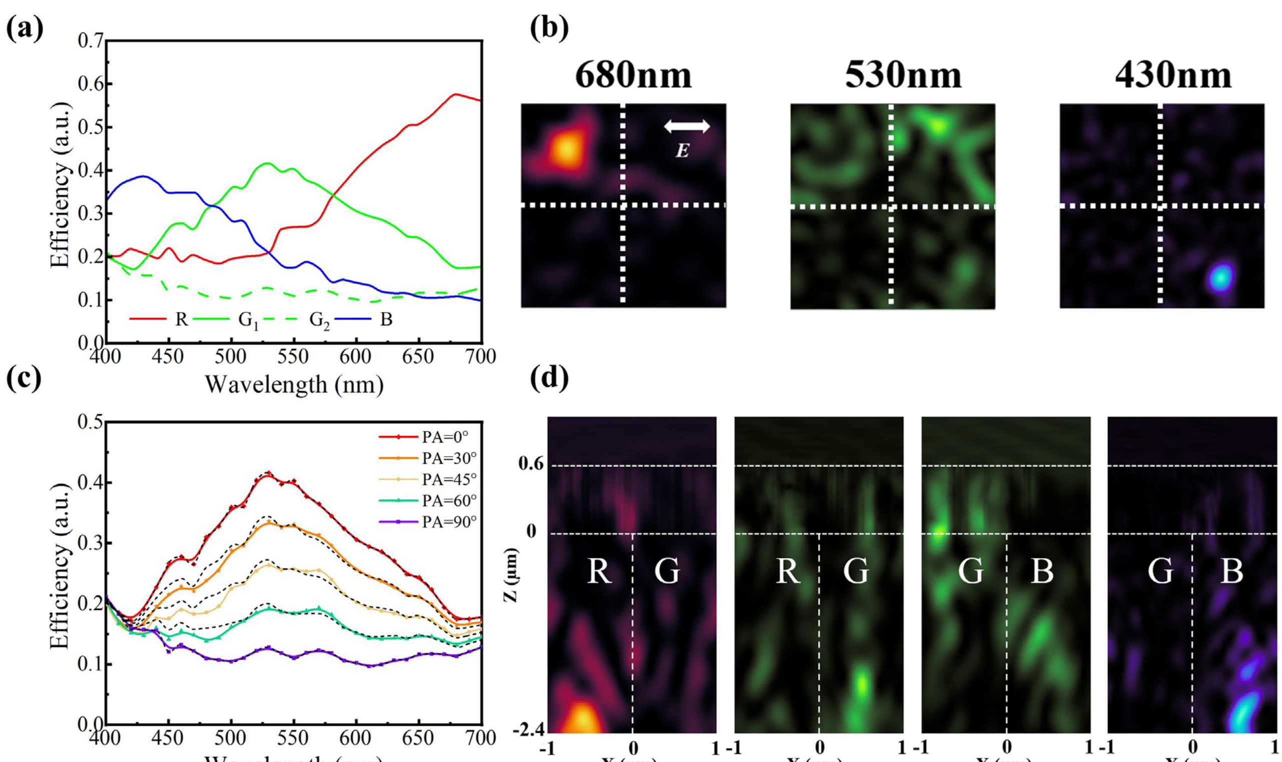

Fig. 3. (a) The simulated spectral responses of color pixels under horizontally polarized illumination. Two green lines represent two green pixels (G_1: upper right quarter; G_2: lower left quarter) in one unit cell. (b) Intensity profiles of detecting plane for three peak wavelengths (680 nm, 530 nm and 430 nm). (c) The simulated (dash lines) and calculated (solid lines) spectral responses of G_1 pixel for different polarization angles (PAs). (d) The lateral sections (XZ plane) of the intensity profiles in (a) for three peak wavelengths at the locations of y=−0.5 μm, −0.75 μm, 0.5 μm and 0.75 μm, respectively.

(i.e. G_2) is approximately 11% over the entire green waveband, which can be ignored and seen as a perturbation of the scattering background [3]. Furthermore, intensity profiles in the detecting plane for three peak wavelengths are given in Fig. 3(b). Note that light of three peak wavelengths is well distributed into three quadrants and another quadrant can hardly collect light. To further observe the transfer of energy flow in the Z direction, the lateral sections (XZ plane) of the intensity profiles for these three peak wavelengths are exhibited in Fig. 3(d), which illustrates that incident lights entering the metasurface are indirectly and effectively routed to the pixels according to the pattern of the metasurface. To quantitatively show the colors instead of pseudo colors in Fig. 3(b), the routing performance is assessed by using color matching functions and depicted in the 1931 CIE chromaticity diagram in Section 2 of **Supplementary Materials**, which roughly conforms to our experiment results below. Fig. 3(c) shows the simulated (black dashed lines) spectral response of the G_1 pixel for different polarizations. The angle formed by the polarization direction and the horizontal direction is defined as the polarization angle (PA). As the structure is symmetrical along the diagonal, the polarization characteristic should conform to Malus' law. Thus, according to the function of Malus' law, we give the efficiencies of the two green pixels under arbitrary PA using the known efficiencies of the green pixels under PA =0, as follows:

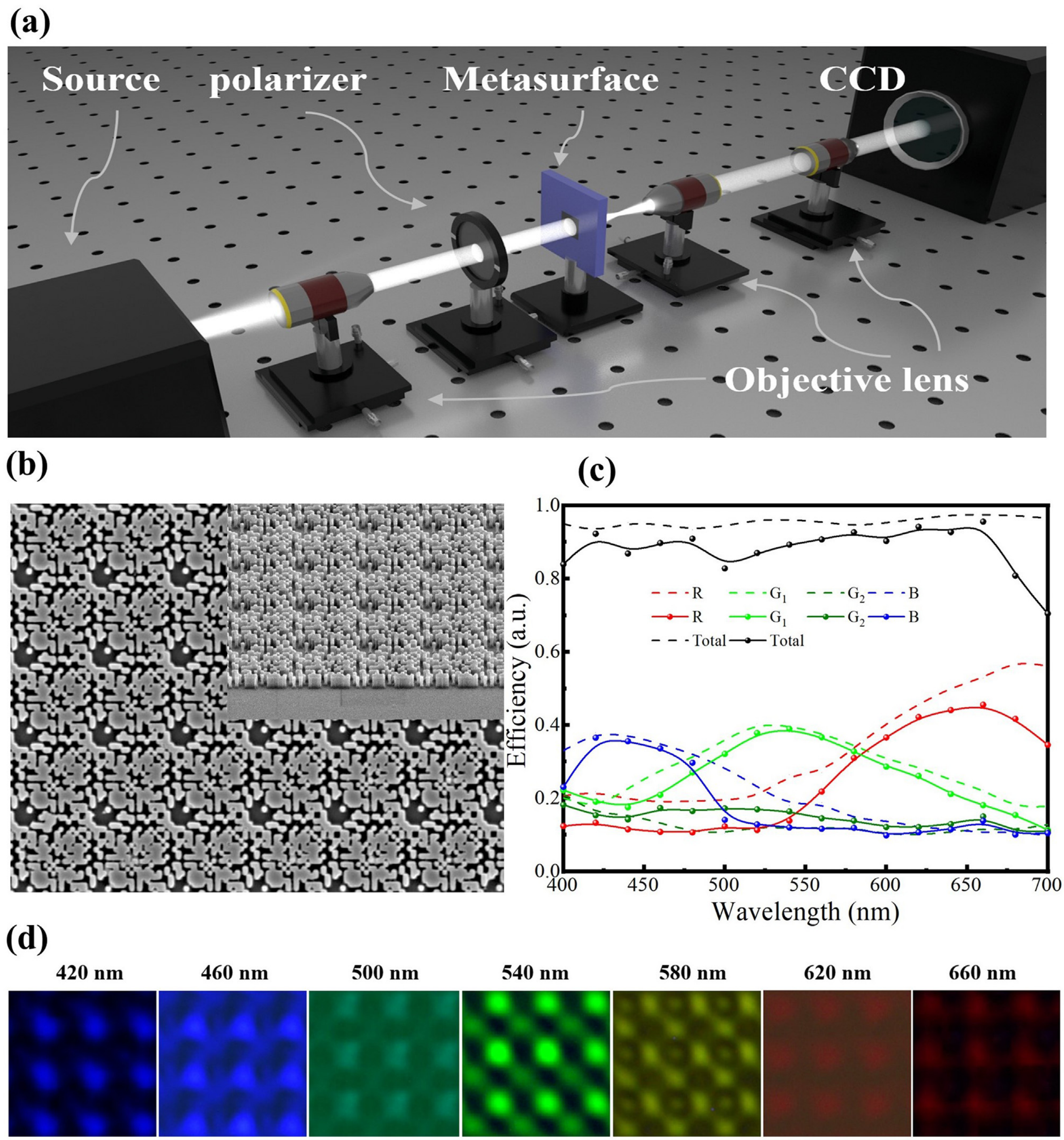

Fig. 4. (a) Schematics of the optical measurement setup. (b) Top-view SEM images of the fabricated metasurface. Inset: side views. Scale bars, 2 μm. (c) Spectral efficiencies of the four (R, G_1, G_2 and B) pixels and the total utilization efficiency when the incident light is horizontally polarized. Solid lines: the measured data. Dotted lines: the theoretical data. (d) Measured intensity profiles at different wavelengths under horizontal polarization.

$$
\begin{aligned}
G_{1,\alpha} &= \left(G_1 - G_2\right)(\cos\alpha)^2 + G_2 \\
G_{2,\alpha} &= \left(G_1 - G_2\right)(\sin\alpha)^2 + G_2,
\end{aligned} \tag{2}
$$

where $G_{1,\alpha}$, $G_{2,\alpha}$ represents the efficiencies of the pixels in the upper right quarter and lower left quarter under linear polarization and PA of α, while G_1, G_2 is that under horizontal polarization (α=0). We calculated the efficiencies of the G_1 pixels under several PAs using Eqs. (2) and depicted them in Fig. 3(c) using color solid lines, which is very consistent with the simulation results. This result illustrates that our MPCR has a great linear polarization response.

Before fabricating the designed metasurface, the influence of the dilation or height fluctuation of the nanostructures on the spectral efficiency is evaluated in Section 3 of **Supplementary Materials** and the simulation results reveal that our structure has great robustness. To experimentally demonstrate the performance of the MPCR, the designed metasurface was fabricated using standard nanofabrication technology, including thin-film deposition, electron beam lithography (EBL), formation of hard etching mask and etching process. Detailed information on the sample fabrication is shown in **Section 4** of **Supplementary Materials**. Fig. 4(b) shows the top-view and side-view scanning electron microscopy (SEM) images of the metasurface. Experimental characterization with the fabricated MPCR sample was performed in the visible regime by using the optical measurement setup in Fig. 4(a). Details are described in **Section 5** of **Supplementary materials**. When collimated polarization lights of different wavelengths are shone on the sample, the intensity profiles of the detecting plane are recorded and presented in Fig. 4(d). It is clear that light of any wavelength in the visible range is efficiently sorted into target pixels, and that the greatest contrast in intensity between pixels occurs precisely at the peak wavelengths. The simulated intensity profiles of different wavelengths are also depicted in Fig. s4 **(Supplementary materials)** for comparison. The difference between the sharp focuses in simulation and the smooth focuses in the experiment is ascribed to the total numerical aperture of the measurement setup. Furthermore, the spectral efficiencies of the four (RG_1G_2B) pixels are calculated in Fig. 4(c) by integrating the intensity of the measured monochromatic intensity profiles over each color pixel for each wavelength and then normalizing by the intensity of incident light over the area of four pixels to eliminate the influence of non-uniform incident light intensity. The MPCR's average total efficiency over the visible regime is 88%, which is 2.6 times higher than the ideal efficiency (33%) of conventional color filters in image sensors. The sorting efficiency is calculated to be 41%, 36% and 32% in the experiment (51%, 38% and 35% in simulation) for R, G and B lights. The measured R-pixel sorting efficiency is lower than the simulated result, which is ascribed to the error introduced by the relatively low light intensity of the incident source in the red waveband. The reason that measured G-pixel and B-pixel efficiencies are slightly lower than the simulated data is that the roughness of the nanostructures causes some undesired light scattering [2].

The polarization response of the MPCR is also characterized according to the light intensity in the detecting plane. Figs. 5(a-c) present the

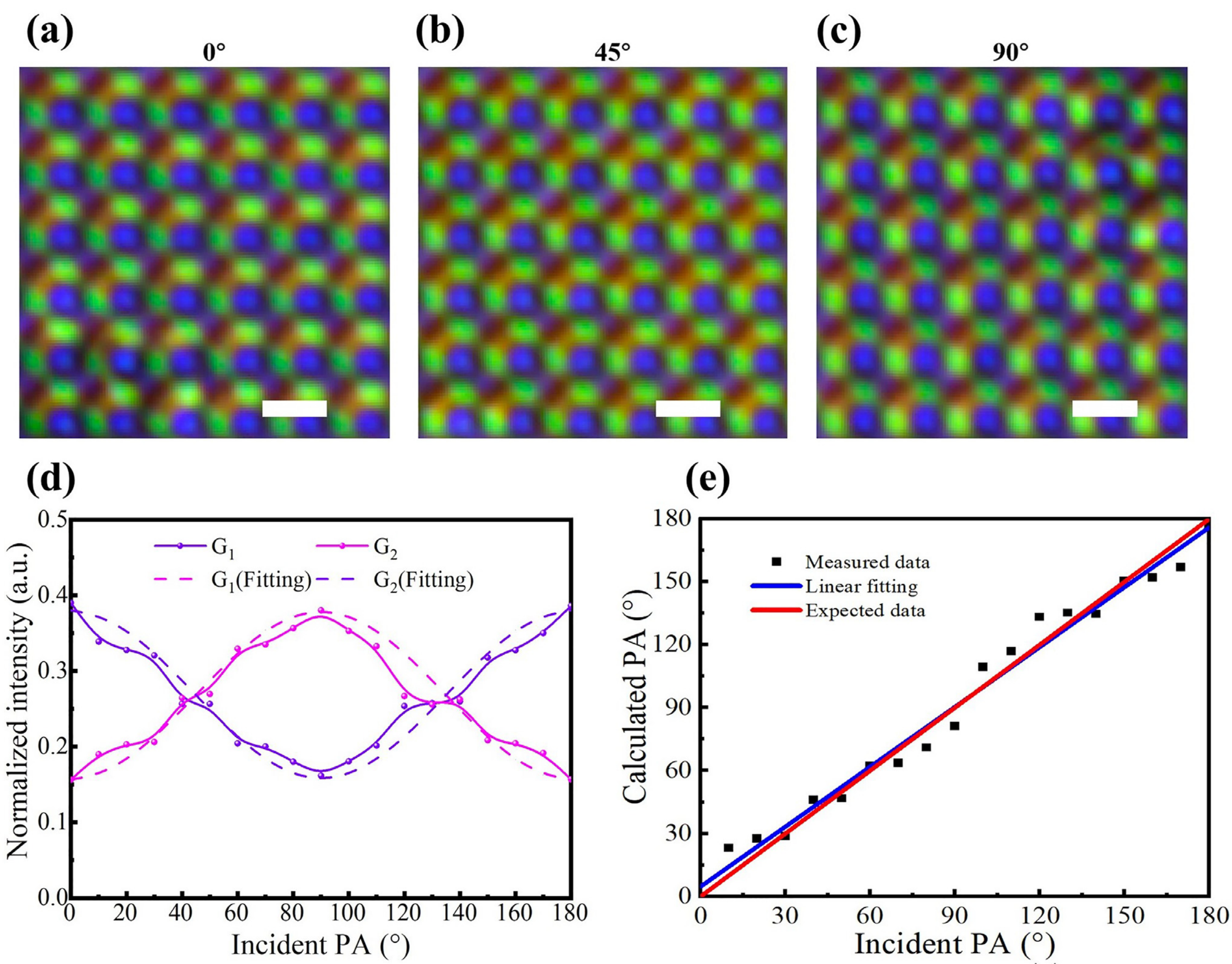

Fig. 5. (a-c) Measured intensity profiles of the MPCR in the detecting plane under linear PA of 0°, 45° and 90°. Scale bar, 2 μm. (d) The calculated normalized intensity of two green pixels (solid lines) and the fitting efficiencies using the Eqs. (2) in the text. (e) Calculated PAs from the measured efficiencies under different directions of linear polarization. Red line: the expected PA value. Point line: the calculated PA value. Blue line: the fitting PA value.

experimental RGGB distributions with the normalized intensity under linear PA of 0°, 45° and 90°, respectively. It shows that R, G and B lights are well focused in each quadrant of the unit cell of the metasurface when the incident light is in the visible waveband and the intensities in the two G pixels are variable according to the directions of polarization. Note that the G_2 pixel under PA of 0° is not dark enough to match the simulated results, which is mainly because the numerical aperture of the collection side is 0.1 which brings the inclined light. The performance of the designed MPCR degrades largely when working under inclined light, which is demonstrated by simulation in **Section 6** of **Supplementary materials**. The intensity contrast (extinction ratio) of G pixels under horizontal or vertical polarization is calculated as 2.5:1 by integrating the intensity of G pixels and normalized by the incident light, while for PA of 45° it is 1.03:1. The degree of polarization P is calculated to be 0.53 in simulation and 0.43 in the experiment according to the equation:

$$P = (I_H - I_V)/(I_H + I_V), \tag{3}$$

where I_H and I_V represent the averaged intensities of the two green pixels (G_1, G_2) over the whole green waveband, respectively. More details about the polarization response are shown in **Section 7** of **Supplementary materials**. Fig. 5(d) depicts the normalized intensity of two G pixels under different PAs, and the fitting data obtained from the Eqs. (2). It can be seen that the two lines essentially meet the relationship of Eq. (2) with the change of PAs. The R and B pixels are polarization-insensitive due to the symmetrical design of the metasurface and the normalized intensities of the two pixels retain approximately 25% and 20%, respectively. Using the normalized intensity of G pixels and the derived PA formula$\alpha = \arctan(\sqrt{(G_{2,\alpha}-G_2)/(G_{1,\alpha}-G_2)})$, the incident PA can be further calculated. The calculated data is shown in Fig. 5(e), which is consistent with the expected PAs. Furthermore, the blue line with the linear function of $y = 0.95x + 4.74$ represents the linear fitting of the measured data. R-square, a correlation coefficient to qualify the linear regression, is calculated to be 98%, demonstrating that the measured data can accurately represent the desired polarization.

3. Conclusions

In summary, we experimentally demonstrate that an MPCR can separate the primary colors used in a color image sensor while also acting as a polarizer to anticipate incident light polarization. In addition to integrating the two functions into a metasurface to realize the miniaturization of a color polarization image sensor, the light utilization efficiency (88% in experiment, 95% in simulation)) and sorting efficiencies (41%, 36% and 32% in the experiment, 51%, 38% and 35% in simulation) are also improved within the micrometer-scale pixel, which is largely significant to the imaging resolution of the polarization image sensor. The incident light's polarization angle can be effectively evaluated using pixel intensity. Furthermore, periodic metasurfaces are highly tractable for industrial mass production due to their resistance to fabrication mistakes. As a result, we believe the MPCR will play a significant role in the development of next-generation color image sensors.

Funding

The authors acknowledge financial support by the National Program on Key Basic Research Project of China (2017YFA0303700), National Natural Science Foundation of China (no. 11,621,091, 11,822,406, 11,834,007, 11,774,164, 11,774,162), the Fundamental Research Funds for the Central Universities (020414380175), and the program A for Outstanding PhD candidate of Nanjing University (202201A003).

Author statement

We the undersigned declare that this manuscript entitled "Metasurface-based polarization color routers" is original, has not been published before and is not currently being considered for publication elsewhere. We confirm that the manuscript has been read and approved by all named authors and that there are no other persons who satisfied the criteria for authorship but are not listed. We further confirm that the order of authors listed in the manuscript has been approved by all of us. We understand that the Corresponding Author is the sole contact for the Editorial process. He is responsible for communicating with the other authors about progress, submissions of revisions and final approval of proofs. Signed by all authors as follows: Xiujuan Zou, Guangxing Gong, Yu Lin, Boyan Fu, Shuming Wang, Shining Zhu and Zhenlin Wang.

Declaration of Competing Interest

The authors have no conflicts to disclose.

Data availability

Data underlying the results presented in this paper are not publicly available at this time but may be obtained from the authors upon reasonable request.

Data will be made available on request.

Supplementary materials

Supplementary material associated with this article can be found, in the online version, at doi:10.1016/j.optlaseng.2022.107472.

References

[1] Chen BH, Wu PC, Su VC, Lai YC, Chu CH, Lee IC, Chen JW, Chen YH, Lan YC, Kuan CH, Tsai DP. GaN metalens for pixel-level full-color routing at visible light. Nano Lett 2017;17(10):6345–52. doi:10.1021/acsnanolett7b03135.
[2] Miyata M, Nemoto N, Shikama K, Kobayashi F, Hashimoto T. Full-color-sorting metalenses for high-sensitivity image sensors. Optica 2021;8(12):1596–604. doi:10.1364/OPTICA.444255.
[3] Camayd-Muñoz P, Ballew C, Roberts G, Faraon A. multifunctional volumetric meta-optics for color and polarization image sensors. Optica 2020;7(4):280–3. doi:10.1364/OPTICA.384228.
[4] Johlin E. Nanophotonic color splitters for high-efficiency imaging. iScience 2021;24(4):102268. doi:10.1016/j.isci.2021.102268.
[5] Nishiwaki S, Nakamura T, Hiramoto M, Fujii T, Suzuki M. Efficient colour splitters for high-pixel-density image sensors. Nat Photonics 2013;7(3):240–6. doi:10.1038/nphoton.2012.345.
[6] Zhao N, Catrysse PB, Fan S. Perfect RGB-IR color routers for sub-wavelength size CMOS image sensor pixels. Adv Photonics Res 2021;2(3):2000048. doi:10.1002/adpr.202000048.
[7] Wang P, Menon R. Ultra-high-sensitivity color imaging via a transparent diffractive-filter array and computational optics. Optica 2015;2(11):933–9. doi:10.1364/OPTICA.2.000933.
[8] Chen Q, Hu X, Wen L, Yu Y, Cumming DR. Nanophotonic image sensors. Small 2016;12(36):4922–35. doi:10.1002/smll.201600528.
[9] Liu Z, Liu X, Xiao Z, Lu C, Wang HQ, Wu Y, Hu X, Liu YC, Zhang H, Zhang X. Integrated nanophotonic wavelength router based on an intelligent algorithm. Optica 2019;6(10):1367–73. doi:10.1364/OPTICA.6.001367.
[10] Miyata M, Nakajima M, Hashimoto T. High-sensitivity color imaging using pixel-scale color splitters based on dielectric metasurfaces. ACS Photonics 2019;6(6):1442–50. doi:10.1021/acsphotonics.9b00042.
[11] Zou X, Zhang Y, Lin R, Gong G, Wang S, Zhu S, Wang Z. Pixel-level Bayer-type colour router based on metasurfaces. Nat Commun 2022;13(1):3288. doi:10.1038/s41467-022-31019-7.
[12] Arbabi A, Horie Y, Bagheri M, Faraon A. Dielectric metasurfaces for complete control of phase and polarization with subwavelength spatial resolution and high transmission. Nat Nanotechnol 2015;10(11):937–43. doi:10.1038/nnano.2015.186.
[13] Kim M, Kim I, Jang J, Lee D, Nam K, Rho J. Active color control in a metasurface by polarization rotation. Appl Sci 2018;8(6):982. doi:10.3390/app8060982.
[14] Rubin NA, Zaidi A, Juhl M, Li RP, Mueller JPB, Devlin RC, Leosson K, Capasso F. Polarization state generation and measurement with a single metasurface. Opt Express 2018;26(17):21455–78. doi:10.1364/OE.26.021455.
[15] Arbabi E, Kamali SM, Arbabi A, Faraon A. Vectorial holograms with a dielectric metasurface: ultimate polarization pattern generation. ACS Photonics 2019;6(11):2712–18. doi:10.1021/acsphotonics.9b00678.
[16] Zang WB, Qin ZF, Yang X, Chen Z, Wang SM, Wang ZL. Polarization generation and manipulation based on nonlinear plasmonic metasurfaces. Adv Opt Mater 2019;7(10):1801747. doi:10.1002/adom.201801747.

[17] Ding F, Chang BD, Wei QS, Huang LL, Guan XW, Bozhevolnyi SI. Versatile polarization generation and manipulation using dielectric metasurfaces. Laser Photonics Rev 2020;14(11):2000116. doi:10.1002/lpor.202000116.
[18] Shi Z, Zhu AY, Li Z, Huang YW, Chen WT, Qiu CW, Capasso F. Continuous angle-tunable birefringence with freeform metasurfaces for arbitrary polarization conversion. Sci Adv 2020;6(23):1–7. doi:10.1126/sciadv.aba3367.
[19] Zhang XQ, Yang SM, Yue WS, Xu Q, Tian CX, Zhang XX, Plum E, Zhang S, Han JG, Zhang WL. Direct polarization measurement using a multiplexed Pancharatnam-Berry metahologram. Optica 2019;6(9):1190–8. doi:10.1364/OPTICA.6.001190.
[20] Deng L, Deng J, Guan Z, Tao J, Chen Y, Yang Y, Zhang D, Tang J, Li Z, Li Z, Yu S, Zheng G, Xu H, Qiu CW, Zhang S. Malus-metasurface-assisted polarization multiplexing. Light Sci Appl 2020;9(1):101–10. doi:10.1038/S41377-020-0327-7.
[21] Yuan Y, Zhang K, Ratni B, Song Q, Ding X, Wu Q, Burokur SN, Genevet P. Independent phase modulation for quadruplex polarization channels enabled by chirality-assisted geometric-phase metasurfaces. Nat Commun 2020;11(1):1–9. doi:10.1038/s41467-020-17773-6.
[22] Arbabi E, Kamali SM, Arbabi A, Faraon A. Full-Stokes imaging polarimetry using dielectric metasurfaces. ACS Photonics 2018;5(8):3132–40. doi:10.1021/acsphotonics.8b00362.
[23] Mueller JPB, Rubin NA, Devlin RC, Groever B, Capasso F. Metasurface polarization optics: independent phase control of arbitrary orthogonal states of polarization. Phys Rev Lett 2017;118(11):113901. doi:10.1103/PhysRevLett.118.113901.
[24] Wu PC, Tsai WY, Chen WT, Huang YW, Chen TY, Chen JW, Liao CY, Chu CH, Sun G, Tsai DP. Versatile polarization generation with an aluminum plasmonic metasurface. Nano Lett 2017;17(1):445–52. doi:10.1021/acs.nanolett.6b04446.
[25] Fan Q, Liu M, Zhang C, Zhu W, Wang Y, Lin P, Yan F, Chen L, Lezec HJ, Lu Y, Agrawal A, Xu T. Independent amplitude control of arbitrary orthogonal states of polarization via dielectric metasurfaces. Phys Rev Lett 2020;125(26):267402. doi:10.1103/PhysRevLett.125.267402.
[26] Hu YQ, Wang XD, Luo XH, Ou XN, Li L, Chen YQ, Yang P, Wang S, Duan HG. All-dielectric metasurfaces for polarization manipulation: principles and emerging applications. Nanophotonics 2020;9(12):3755–80. doi:10.1515/nanoph-2020-0220.
[27] Intaravanne Y, Chen XZ. Recent advances in optical metasurfaces for polarization detection and engineered polarization profiles. Nanophotonics 2020;9(5):1003–14. doi:10.1515/nanoph-2019-0479.
[28] Chen WT, Yang KY, Wang CM, Huang YW, Sun G, Chiang ID, Liao CY, Hsu WL, Lin HT, Sun S, Zhou L, Liu AQ, Tsai DP. High-efficiency broadband metahologram with polarization-controlled dual images. Nano Lett 2014;14(1):225–30. doi:10.1021/nl403811d.
[29] Wen D, Yue F, Li G, Zheng G, Chan K, Chen S, Chen M, Li KF, Wong PW, Cheah KW, Pun EY, Zhang S, Chen X. Helicity multiplexed broadband metasurface holograms. Nat Commun 2015;6(1):8241. doi:10.1038/ncomms9241.
[30] Khorasaninejad M, Ambrosio A, Kanhaiya P, Capasso F. Broadband and chiral binary dielectric meta-holograms. Sci Adv 2016;2(5):e1501258. doi:10.1126/sciadv.1501258.
[31] Devlin RC, Ambrosio A, Rubin NA, Mueller JPB, Capasso F. Arbitrary spin-to-orbital angular momentum conversion of light. Science 2017;358(6365):896–901. doi:10.1126/science.aao5392.
[32] Stav T, Faerman A, Maguid E, Oren D, Kleiner V, Hasman E, Segev M. Quantum entanglement of the spin and orbital angular momentum of photons using metamaterials. Science 2018;361(6407):1101–4. doi:10.1126/science.aat9042.
[33] Huang YW, Rubin NA, Ambrosio A, Shi Z, Devlin RC, Qiu CW, Capasso F. Versatile total angular momentum generation using cascaded J-plates. Opt Express 2019;27(5):7469–84. doi:10.1364/OE.27.007469.
[34] Sroor H, Huang YW, Sephton B, Naidoo D, Valles A, Ginis V, Qiu CW, Ambrosio A, Capasso F, Forbes A. High-purity orbital angular momentum states from a visible metasurface laser. Nat Photonics 2020;14(8):498–503. doi:10.1038/s41566-020-0623-z.
[35] Guo Y, Zhang S, Pu M, He Q, Jin J, Xu M, Zhang Y, Gao P, Luo X. Spin-decoupled metasurface for simultaneous detection of spin and orbital angular momenta via momentum transformation. Light Sci Appl 2021;10(1):63. doi:10.1038/s41377-021-00497-7.
[36] Yan C, Li X, Pu MB, Ma XL, Zhang F, Gao P, Liu KP, Luo XG. Midinfrared real-time polarization imaging with all-dielectric metasurfaces. Appl Phys Lett 2019;114(16):161904. doi:10.1063/1.5091475.
[37] Zang X, Dong F, Yue F, Zhang C, Xu L, Song Z, Chen M, Chen PY, Buller GS, Zhu Y, Zhuang S, Chu W, Zhang S, Chen X. Polarization encoded color image embedded in a dielectric metasurface. Adv Mater 2018;30(21):e1707499. doi:10.1002/adma.201707499.
[38] Courtier G, Lapray PJ, Thomas JB, Farup I. Correlations in joint spectral and polarization imaging. Sensors-Basel 2020;21(1):6. doi:10.3390/s21010006.
[39] Sarkar M, Bello DSSSS, Van Hoof C, Theuwissen A. Integrated polarization analyzing CMOS image sensor for material classification. IEEE Sens J 2011;11(8):1692–703. doi:10.1109/JSEN.2010.2095003.
[40] Wu PC, Sokhoyan R, Shirmanesh GK, Cheng WH, Atwater HA. Near-Infrared active metasurface for dynamic polarization conversion. Adv Opt Mater 2021;9(16):2100230. doi:10.1002/adom.202100230.
[41] Ellenbogen T, Seo K, Crozier KB. Chromatic plasmonic polarizers for active visible color filtering and polarimetry. Nano Lett 2012;12(2):1026–31. doi:10.1021/nl204257g.
[42] Shen B, Wang P, Polson R, Menon R. Ultra-high-efficiency metamaterial polarizer. Optica 2014;1(5):356–60. doi:10.1364/OPTICA.1.000356.
[43] Yuan Y, Sun S, Chen Y, Zhang K, Ding X, Ratni B, Wu Q, Burokur SN, Qiu CW. A fully phase-modulated metasurface as an energy-controllable circular polarization router. Adv Sci 2020;7(18):2001437. doi:10.1002/advs.202001437.
[44] Fan Y, Xu Y, Qiu M, Jin W, Zhang L, Lam EY, Tsai DP, Lei D. Phase-controlled metasurface design via optimized genetic algorithm. Nanophotonics 2020;9(12):3931–9. doi:10.1515/nanoph-2020-0132.
[45] Zhu RC, Qiu TS, Wang JF, Sui S, Li YF, Feng MD, Ma H, Qu SB. Multiplexing the aperture of a metasurface: inverse design via deep-learning-forward genetic algorithm. J Phys D Appl Phys 2020;53(45):455002. doi:10.1088/1361-6463/aba64f.